



Article

Molecular Layer Doping ZnO Films as a Novel Approach to Resistive Oxygen Sensors

Wojciech Bulowski ^{1,2,*}, Robert P. Socha ^{1,3}, Anna Drabczyk ¹, Patryk Kasza ¹, Piotr Panek ⁴ and Marek Wojnicki ^{1,2,*}

- CBRTP SA Research and Development Center of Technology for Industry, Ludwika Waryńskiego 3A, 00-645 Warszawa, Poland
- Faculty of Non-Ferrous Metals, AGH University of Krakow, Al. Mickiewicza 30, 30-059 Kraków, Poland
- ³ Jerzy Haber Institute of Catalysis and Surface Chemistry, Polish Academy of Sciences, Niezapominajek 8, 30-239 Kraków, Poland
- Institute of Metallurgy and Materials Science, Polish Academy of Sciences, 25 Reymonta St., 30-059 Kraków, Poland
- * Correspondence: wbulowski@agh.edu.pl (W.B.); marekw@agh.edu.pl (M.W.)

Abstract: In the modern world, gas sensors play a crucial role in sectors such as high-tech industries, medicine, and environmental monitoring. Among these fields, oxygen sensors are the most important. There are several types of oxygen sensors, including optical, magnetic, Schottky diode, and resistive (or chemoresistive) ones. Currently, most oxygen-resistive sensors (ORSs) described in the literature are fabricated as thick layers, typically deposited via screen printing, and they operate at high temperatures, often exceeding 700 °C. This work presents a novel approach utilizing atomic layer deposition (ALD) to create very thin layers. Combined with appropriate doping, this method aims to reduce the energy consumption of the sensors by lowering both the mass requiring heating and the operating temperature. The device fabricated using the proposed process demonstrates a response of 88.21 at a relatively low temperature of 450 °C, highlighting its potential in ORS applications based on doped ALD thin films.

Keywords: gas sensor; doped zinc oxide; atomic layer deposition



Academic Editor: Domenico Caputo

Received: 3 January 2025 Revised: 25 January 2025 Accepted: 31 January 2025 Published: 2 February 2025

Citation: Bulowski, W.; Socha, R.P.; Drabczyk, A.; Kasza, P.; Panek, P.; Wojnicki, M. Molecular Layer Doping ZnO Films as a Novel Approach to Resistive Oxygen Sensors. *Electronics* 2025, 14, 595. https://doi.org/ 10.3390/electronics14030595

Copyright: © 2025 by the authors. Licensee MDPI, Basel, Switzerland. This article is an open access article distributed under the terms and conditions of the Creative Commons Attribution (CC BY) license (https://creativecommons.org/licenses/by/4.0/).

1. Introduction

The applications of oxygen include a wide range of industries including medicine [1], environmental monitoring [2] and industrial processes [3]. This is because of the ability of such sensors to accurately measure oxygen concentration under various conditions [4]. Measuring oxygen concentration is crucial for ensuring the efficiency and safety of processes, such as controlling combustion efficiency in engines [5]. In inert gas storage facilities, the presence of oxygen can lead to adverse chemical reactions, which highlights the importance of accurate and reliable sensors in such systems. The application of oxygen sensors also extends beyond traditional sectors—they are becoming an essential part of advanced technologies in aviation, aerospace [6] and modern energy systems [7]. Developments in sensor technology, combined with increasing demands for precision and durability, are constantly driving intensive investigations in this area.

Oxygen sensors can be divided into paramagnetic, electrochemical, optical and resistance types depending on the operation mechanism [8]. Each of these types demonstrates both benefits and limitations, which makes them adequate for various applications. Paramagnetic sensors due to their magnetic properties are particularly useful in applications

requiring high accuracy in chemical laboratories [9], while electrochemical ones are compact and show high precision, but their operation can be limited in harsh environments [10]. This type of oxygen sensors is widely used, for example, in medicine [11]. In turn, optical sensors are gaining popularity due to their non-invasiveness, stability and resistance to environmental disturbances [12–14]. Resistive sensors, on the other hand, are ideal for industrial applications, such as monitoring flue gases or combustion processes in smelter furnaces, due to their simple design and ability to operate at high temperatures [15]. Among the aforementioned oxygen sensor types, resistive oxygen sensors constitute a promising solution for applications requiring operation in extreme conditions, such as high temperatures or the presence of corrosive gases. Their operation is based on the change in the electrical resistance of an active material in response to the adsorption and desorption of oxygen molecules on its surface [8,15]. The materials most commonly used in such sensors are semiconducting metal oxides such as ZnO, SnO₂ or TiO₂. Their electronic properties allow them to respond sensitively to changes in ambient oxygen concentration, and the crystal structure of these materials allows for the modification of their properties by doping or forming nanostructures. As a result, resistive sensors can be customized for a variety of applications, from monitoring industrial combustion processes to air quality control systems [16–18].

Challenges faced by resistive sensors can limit their effectiveness. The literature also points to the degradation of the active material at high temperatures, which can result in a decrease in sensor sensitivity and durability. Another challenge for resistive sensors is their long-term stability under harsh environmental conditions. Operating at high temperatures can lead to sintering of the active material, which reduces its active surface area and affects the repeatability of measurement results. For example, temperature cycling can cause the growth of crystalline grains in metal oxides, which negatively affects their ability to adsorb oxygen. In addition, if the material is not properly matched to the operating conditions, corrosion processes can accelerate sensor degradation [19–21].

Today's challenges in gas detection, associated with the growing demand for precise, durable and energy-efficient sensors, are driving the search for new materials and technologies. Of particular importance are solutions that combine high selectivity and sensitivity with the ability to integrate into modern electronic systems. Technological challenges include not only improving selectivity and sensitivity but also long-term stability and the ability to operate in varying environmental conditions [22,23]. In recent years, particular attention has been given to the development of sensors resistant to interferences caused by water vapor and other gases present in the measurement environment, which can affect the accuracy of oxygen measurements; hence, this aspect remains one of the primary challenges in designing these devices. The reliability of oxygen sensors under dynamic conditions, such as fluctuating temperatures and humidity levels, has become a critical focus of research. Interferences arising from the presence of water vapor or carbon dioxide can significantly limit the effectiveness of sensors [24,25]. Studies have shown that metal oxides exhibit the competitive adsorption of oxygen and water in humid environments, leading to the falsification of results. In addition, their response time and sensitivity can vary significantly depending on operating conditions such as temperature and pressure [26–28]. In response to these challenges, some strategies have been developed so far. These strategies involve two main approaches, i.e., the pre-treatment of analyzed mixtures aimed at reducing the water content and the modification of sensors so as to disfavor water adsorption or promote the adsorption of other compounds [29–31]. The modification of sensors includes doping using various elements like transition metals, noble metals or lanthanide ones [32,33]. Another strategy that can be applied is the integration of sensors with a hydrophobic membrane based on, among others, polymers [34,35], molecular sieves

or mesoporous nanoboxes [36]. However, these approaches often involve additional costs or technological limitations, such as complex fabrication processes or limited scalability for mass production. Addressing these limitations requires the integration of novel materials and precise fabrication techniques to enhance sensor performance while maintaining cost-efficiency.

Recent advancements in the field of oxygen sensors have focused on improving sensitivity, selectivity and long-term stability through the development of nanostructured materials and hybrid composites. A significant breakthrough has been the application of ZnO-based nanostructures, such as nanowires [37,38], nanotubes [39], and nano-thin films [40,41], which significantly enhance the surface-to-volume ratio, facilitating more efficient gas adsorption. The incorporation of dopants and the creation of heterostructures, such as ZnO combined with reduced graphene oxide [42] or other two-dimensional materials [43], have further demonstrated breakthroughs in reducing interference from competing gases. Thin-film deposition techniques, particularly atomic layer deposition (ALD), have played a pivotal role in advancing these technologies by enabling the precise control of chemical composition and layer thickness, which improves sensor operational parameters. ALD stands out for its ability to deposit ultrathin layers with atomic-level precision, ensuring uniform structure, enhanced material properties, and better performance in harsh environmental conditions. Moreover, ALD enables the integration of advanced doping strategies, offering unparalleled opportunities to fine-tune material properties for specific sensing requirements while ensuring scalability for industrial applications [44–47].

A key factor in the advancement of oxygen sensor technologies is the choice of fabrication method, as each technique offers distinct advantages and limitations. Thick-film technologies, such as screen printing, are widely used due to their simplicity, low cost, and compatibility with a range of substrates. However, these methods often result in films with poor uniformity, limited control over thickness, and the presence of structural defects, which can negatively impact sensor performance [48–50]. Physical vapor deposition (PVD), including techniques like sputtering and evaporation, provides higher precision and better control over thin-film thickness compared to thick-film methods, but it may struggle with uniformity over large areas and requires higher vacuum conditions, increasing operational costs [51,52]. Chemical vapor deposition (CVD) offers improved scalability and the ability to coat complex geometries, yet it can be hindered by high material usage, potential contamination, and limited control at the atomic level [53,54]. In contrast, ALD surpasses these methods by offering atomic-level precision and unparalleled control over the thickness, composition, and uniformity of thin films. Unlike thick-film methods, ALD produces defect-free and highly uniform layers, ensuring consistent sensor performance across the substrate. Compared to PVD and CVD, ALD operates at lower temperatures and allows for conformal coatings on intricate surfaces, making it particularly suitable for advanced sensor designs. Additionally, ALD's layer-by-layer growth process minimizes material waste and enables the precise incorporation of dopants, which is essential for tailoring the electronic and surface properties of the active layer. The scalability of ALD, combined with its ability to produce high-quality films at industrial scales, positions it as a transformative technology, addressing the limitations of traditional methods while enhancing sensor sensitivity, selectivity, and long-term stability.

Oxygen sensors based on ZnO thin films find broad applications in various fields, including environmental monitoring, the automotive industry, industrial production, and medicine. Their ability to precisely detect changes in oxygen concentration enables the optimization of technological processes, control of exhaust emissions, and ensuring safety in industrial conditions. ZnO layers for gas sensing applications can be synthesized using various methods, such as chemical vapor deposition (CVD) [55], physical vapor deposition

(PVD) [56], hydrothermal synthesis [57], microwave-assisted hydrothermal synthesis [37], sol–gel processing [58], successive ion layer adsorption and reaction [59], magnetron sputtering [60], or sputtering followed by thermal oxidation in dry air [61]. However, while magnetron sputtering is cost-effective, it is also limited by batch size, has difficulty with coating complex surfaces, and has less precise doping. In turn, CVD generates harmful by-products and lacks full conformal coating. ALD, as an advanced variation in CVD, addresses these limitations by offering full conformality on complex surfaces, precise doping control, and significantly less harmful waste production. A schematic comparison of magnetron sputtering, CVD and ALD is illustrated below in Figure 1.

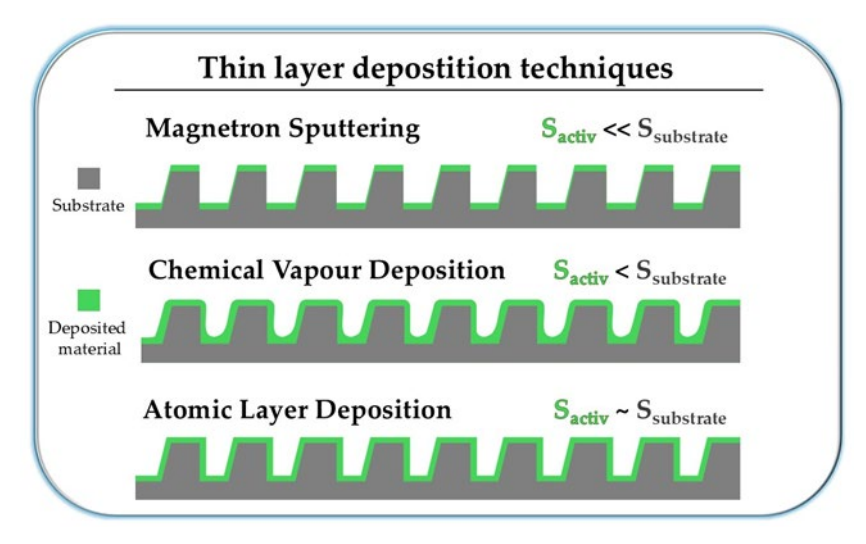


Figure 1. Thin-layer deposition techniques. Images adapted with permission from [8] MDPI, 2024.

ZnO (zinc oxide) layers deposited by the ALD method seem particularly promising. ZnO layers are characterized by the possibility of fine-tuning their electrical and structural properties through changes in composition, thickness and deposition techniques [62–64]. The ALD technology allows for the controlled atom-by-atom deposition of materials, which ensures homogeneity and stability of the resulting layers, even at nanometer thicknesses. Such materials are distinguished by their wide energy gap, good chemical stability and piezoelectric properties, making them suitable for oxygen-sensing applications that require reliability under varying environmental conditions [65–67]. However, there are challenges associated with the limitations of ZnO itself, such as instability over longer lifetimes and susceptibility to degradation under harsh environmental conditions. Hence, there are strategies that can mitigate these issues, such as doping active materials with elements that enhance sensor stability and selectivity. For example, doping with tin, germanium, zirconium or niobium can improve the adsorption properties of metal oxides and their resistance to sintering. Doping with these elements can also improve the sensitivity of sensors by increasing the number of active centers on the surface of the material [22,68,69].

To address the challenges outlined above, this study focuses on leveraging atomic layer deposition and molecular doping techniques to design ZnO-based oxygen sensors with enhanced sensitivity, selectivity, and stability under real-world conditions. The aim of this study is to investigate the impact of molecular doping of ZnO thin films on their sensor properties for oxygen detection. The research involves the use of the ALD technique, a detailed physicochemical analysis and testing under conditions close to real-world applications. By employing advanced characterization techniques, this work explores the interplay between doping levels, film thickness and environmental factors in determining sensor performance. This work aims to fill the gap in the literature concerning the effective design of sensors resistant to environmental interferences, thereby contributing to the ad-

vancement of modern gas detection technologies. This study introduces a novel approach to enhancing ZnO-based oxygen sensors by integrating molecular layer doping with ALD. The precision offered by ALD enables the creation of ultrathin, uniform ZnO films, while molecular layer doping allows for atomic-level tailoring of electronic and surface properties through controlled doping with elements such as germanium, niobium, tin and zirconium. This dual-strategy fabrication method improves sensitivity and selectivity by creating optimized active sites for oxygen adsorption and reducing interference from competing gases like water vapor and carbon dioxide. Additionally, the tailored electronic structure enhances charge carrier mobility, resulting in faster response times and greater stability under real-world conditions. This approach addresses critical limitations of traditional doping techniques and provides a scalable, industrially applicable solution for the development of high-performance gas sensors. As part of the ongoing work, undoped ZnO layers and doped ones using elements such as tin, germanium, zirconium and niobium have been obtained. The fabricated materials were subsequently subjected to detailed physicochemical characterization, using techniques such as UV-Vis spectroscopy to determine the energy gap and XPS analysis to examine the chemical composition and bonding states of the dopants within the ZnO layers. Additionally, work function analysis and the Hall effect measurements provided information on the electrical properties, including carrier concentration and mobility. Finally, the sensory properties of obtained layers were evaluated to check their application potential in oxygen sensing.

2. Materials and Methods

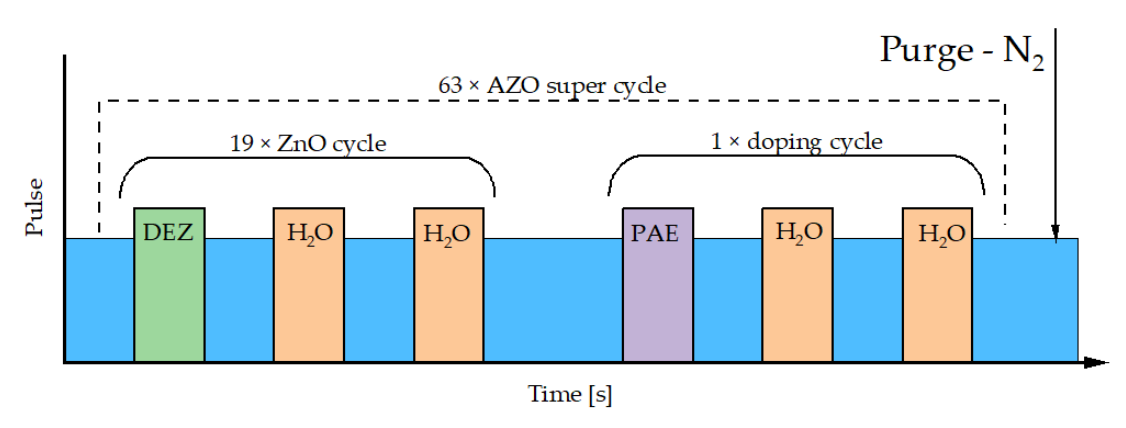
2.1. Fabrication of the Thin Films

2.1.1. Atomic Layer Deposition (ALD)

In this study, ALD was employed for preparing ZnO and doped ZnO layers, which was performed using an ALD reactor (Beneq P400A ALD system, Espoo, Finland). Depositions were conducted at a temperature of 200 °C and a chamber pressure of approximately 1 mbar with constant nitrogen flow of 2.5 slm (99.999% purity, PSA Nitrogen Gas Generator, Parker). Diethylzinc (DEZ) (99%, Lanxess Organometallics GmbH, Bergkamen, Germany) was used as the zinc precursor for ALD. Tetramethoxygermanium (98%, Gelest, Inc., Morrisville, NC, USA), tetrakis(dimethylamino)tin(IV) (98%, abcr GmbH, Karlsruhe, Germany), tetrakis(dimethylamino)zirconium(IV) (98%, abcr GmbH) and niobium ethoxide(V) (99.95%, Merck, Darmstadt, Germany) were used for doping with germanium, tin, zirconium and niobium, respectively. High-purity deionized (DI) water was used as the oxygen precursor to form oxides.

The ALD consists of repeating cycles of alternating pulses of metal–organic and oxygen precursors. For each cycle, one pulse of zinc precursor (DEZ) is followed by two pulses of water. To acquire 5% doping level in 1 of every 20 cycles, DEZ is replaced by the precursor of the additive element (PAE). The precursor pulse time was fixed at 0.3 s for DEZ and additive precursors, and 0.5 s for water, wherein after each precursor, a 5 s pulse of purge step (N₂) was delivered. To obtain 100 nm layers, the super cycle (19 cycles of ZnO and 1 doping cycle) was repeated 63 times (Figure 2).

The depositions were conducted on 180 μ m thick ultra-flat single-side polished silicon wafers <100> (Alpha Nanotech Inc., Vancouver, BC, Canada) for thickness and XPS measurements and on 2 mm thick high-transparent quartz substrates (Helma, Müllheim, Germany) for optical and electrical measurements. Quartz glass was chosen as the substrate for the sensor device because of its non-conductive properties.



PAE - precursor of additive element (Ge, Sn, Zr, Nb precursors)

Figure 2. ALD process of doped ZnO layers.

Before loading to the ALD chamber, substrates were cleaned; the cleaning procedure applied is described in our previous paper [70]. Firstly, silicon wafers were rinsed with isopropanol. After cleaning, substrates were also activated by argon plasma with the following parameters: RF, 120 W, and 2 min (Diener tetra 30, Ebhaussen, Germany).

After deposition, samples were annealed at 500 °C for 3 h (in air) in order to fill the oxygen vacancies and prepare obtained devices for oxygen sensing in high temperatures (Figure 3).

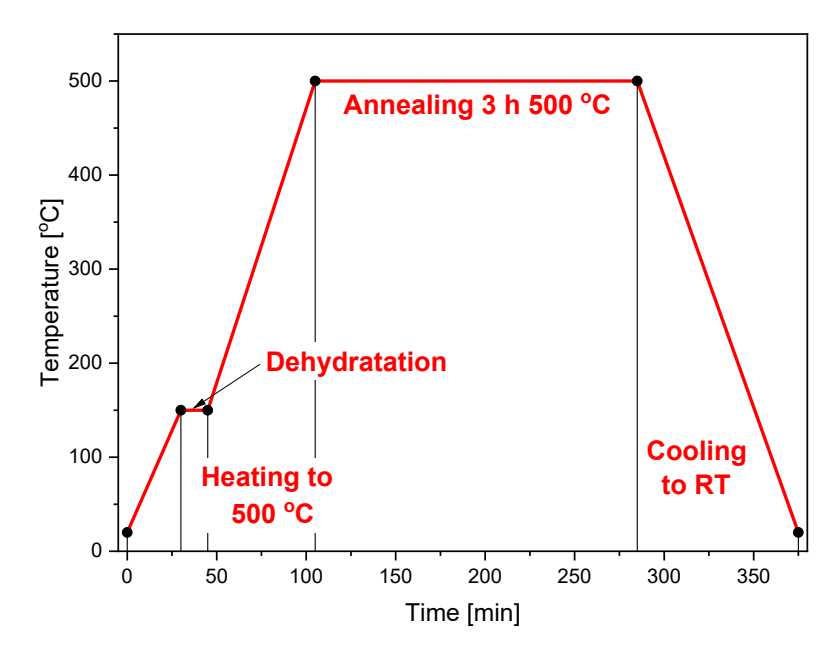


Figure 3. Annealing procedure of prepared samples.

2.1.2. Physical Vapor Deposition (PVD)

Physical vapor deposition was used for the deposition of gold electrodes to provide good electrical contact to fabricated sensor devices. The thickness of deposited electrodes was approximately 50 nm.

2.2. Film Characterization

2.2.1. Ellipsometry

The nominal thickness of obtained layers was measured using Sentech SE400adv PV Multi-Angle Laser Ellipsometer. The analyses were conducted at an incident angle of 70°

with class 1 (632.8 nm wavelength) HeNe laser (diameter of laser beam 1 mm). For optical measurements, the model Air/ZnO/Si (<100>) stack was used.

2.2.2. X-Ray Photoelectron Spectroscopy (XPS)

The X-ray photoelectron spectra (XPS) were acquired using hemispherical analyzer EA 15 (PREVAC) equipped with X-ray source RS 40B1 (PREVAC). The measurements were performed using Al K α (1486.6 eV) radiation and an analyzer pass energy of 100 eV. The spectra ware recorded in normal emission geometry with an energy resolution of 0.9 eV. The spectrometer was calibrated with the Ag, Au and Cu foil according to ISO 15472:2010 standard [71]. The ultra-high vacuum (UHV) conditions of 1×10^{-9} mbar were maintained during the measurements. The area of analysis was approximately 3 mm² and depth of analysis was about 8 nm. The spectra were analyzed with the use of CasaXPS 2.3.24PR software. The electron binding energy (BE) scale was calibrated for the maximum intensity of C 1s peak at 285.0 eV. The Shirley-type spectrum background was used. The highly resolved spectra were deconvoluted with Voigt function (Gauss to Lorentz profile ratio of 70:30).

2.2.3. Optical Properties

The band gaps were calculated from transmittance and reflectance of doped ZnO films using Tauc plots. In order to obtain transmittance and reflectance of prepared samples, Shimadzu UV-2600i UV-Vis spectrometer was used in a range of 220–1400 nm.

2.2.4. Electrical Properties

The electrical properties of obtained doped ZnO layers were measured using Hall effect measurement system ECOPIA HMS-5500 (Anyang, Republic of Korea). Measurements were performed at room temperature.

2.2.5. Kelvin Probe Force Microscopy (KPFM)

The work function of the doped ZnO films was measured with Kelvin Probe with golden mech probe at height of 0.2 mm. First, the measurements of the contact potential difference (CPD) between the measuring tip and the surface of the film were carried out. Then, the work function ϕ of the film was calculated as follows:

$$CPD = \frac{(\varphi - \varphi_{Au_{RE}})}{e} \tag{1}$$

where e is the elementary charge, 1.6×10^{-19} C. The ϕ_{Au} value was obtained by calibration of the probe with HOPG (highly oriented pyrolytic graphite). After calibration, a value of $\phi = 4.815$ eV was adopted for the gold probe.

2.2.6. Sensing Properties

The sensing abilities of fabricated devices were measured by the constructed setup presented in Figure 4.

The setup was composed of a hot plate (IKA C-MAG HS 7) as a heat source, tabletop multimeter (Keithley 2700) for resistance measurement and a measurement chamber with high gas flow (7.5 slm). Gas flow, its pressure and composition were regulated by rotameter and electro valve. All of the system components were controlled by a computer program.

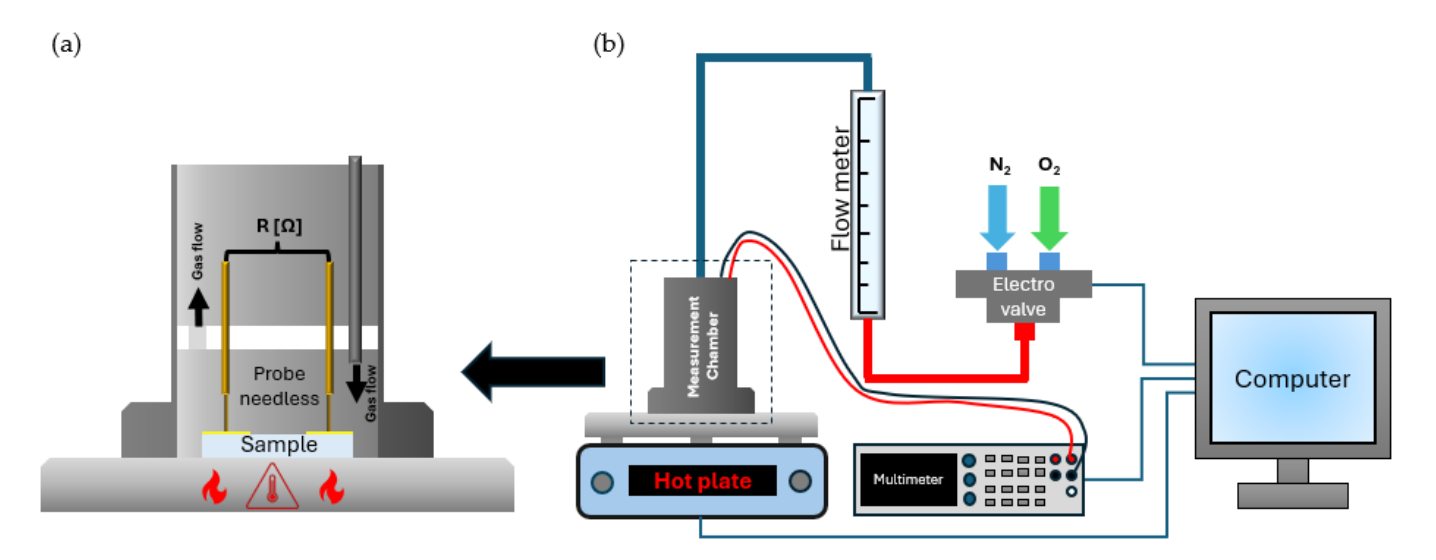


Figure 4. (a) High flow measurement chamber and (b) whole-sensor-measurement setup.

3. Results and Discussion

The thickness of the deposited layers measured using ellipsometry is shown in Table 1. To designate proper a refractive index (RI), a multi-angle mode was used $(40, 50, 60, 70^{\circ})$ angles). For GZO and NZO, the RI was almost the same with that of ZnO, wherein tin doping caused the biggest change in RI, i.e., its value was 2.2140 for SZO layers. The differences in the RI change between the used dopants could be related to different effective doping levels or the way in which the additives are located in the crystal lattice.

Table 1. Thickness and refractive index o	f obtained lave	r.
--	-----------------	----

•	Sample Name	Doping *	Thickness	Refractive index **
	ZnO	-	104.6 nm	1.9888
	GZO	5% Ge	106.4 nm	1.9886
	SZO	5% Sn	90.6 nm	2.2140
	ZZO	5% Zr	101.8 nm	1.9476
	NZO	5% Nb	96.4 nm	1.9874

^{*} Percent of ALD doping cycles. ** Refractive index at 632.8 nm.

Based on the performed studies, it turned out that doping does not have a significant influence on the layer thickness; again, only SZO stands out with a 90.6 nm thick layer, which is 14 nm thinner than the pristine ZnO layer.

The introduction of dopants into the ZnO lattice significantly impacts the refractive index (RI) through mechanisms such as lattice distortion, modifications to the electronic structure and defect formation [72–74]. Ions with radii differing significantly from those of the host ion (Zn^{2+}) can induce lattice strain, which alters the material's structural and electronic properties [75]. This strain can lead to the formation of secondary phases or agglomerates with distinct dielectric properties, contributing to changes in the dielectric constant (ϵr) [76,77] and, consequently, the RI. The dielectric constant, a measure of a material's ability to polarize in response to an electric field [78], is further influenced by changes in the electronic structure and interactions between dopants and the lattice. Lattice defects introduced by dopants, as well as variations in carrier concentration, can also enhance the material's polarizability [79], amplifying these effects, and further modifying the dielectric constant and RI.

The electronic structure also changes, as observed in germanium (Ge)-doped ZnO, where the Burstein–Moss effect shifts the Fermi level, increasing the bandgap [70,80] and RI. Furthermore, dopants like niobium (Nb) introduce localized defect states [81], subtly impacting the RI by enhancing lattice polarizability.

Thanks to the specificity of the ALD technique, molecular doping in a form of a single atomic layer is feasible. Molecular doping in combination with a very uniform distribution of additive elements along whole surfaces results in very efficient doping possibilities, where every doped atom actively interacts with the matrix. In the case of ALD, a low percent doping level is usually enough to obtain good results. In this article, a 5% percent doping level executed by the deposition cycle control (1 cycle of PAE + water for each 19 cycle of DEZ + water) was chosen. The choice was made based on the doping level of popular ZnO-doped layer AZO (Al-doped ZnO), which is usually 5% based on our previous experiences [70,82].

To determine the efficiency of doping and the dopant content in each tested variant, XPS measurements were conducted. The results of this study are presented in Figure 5.

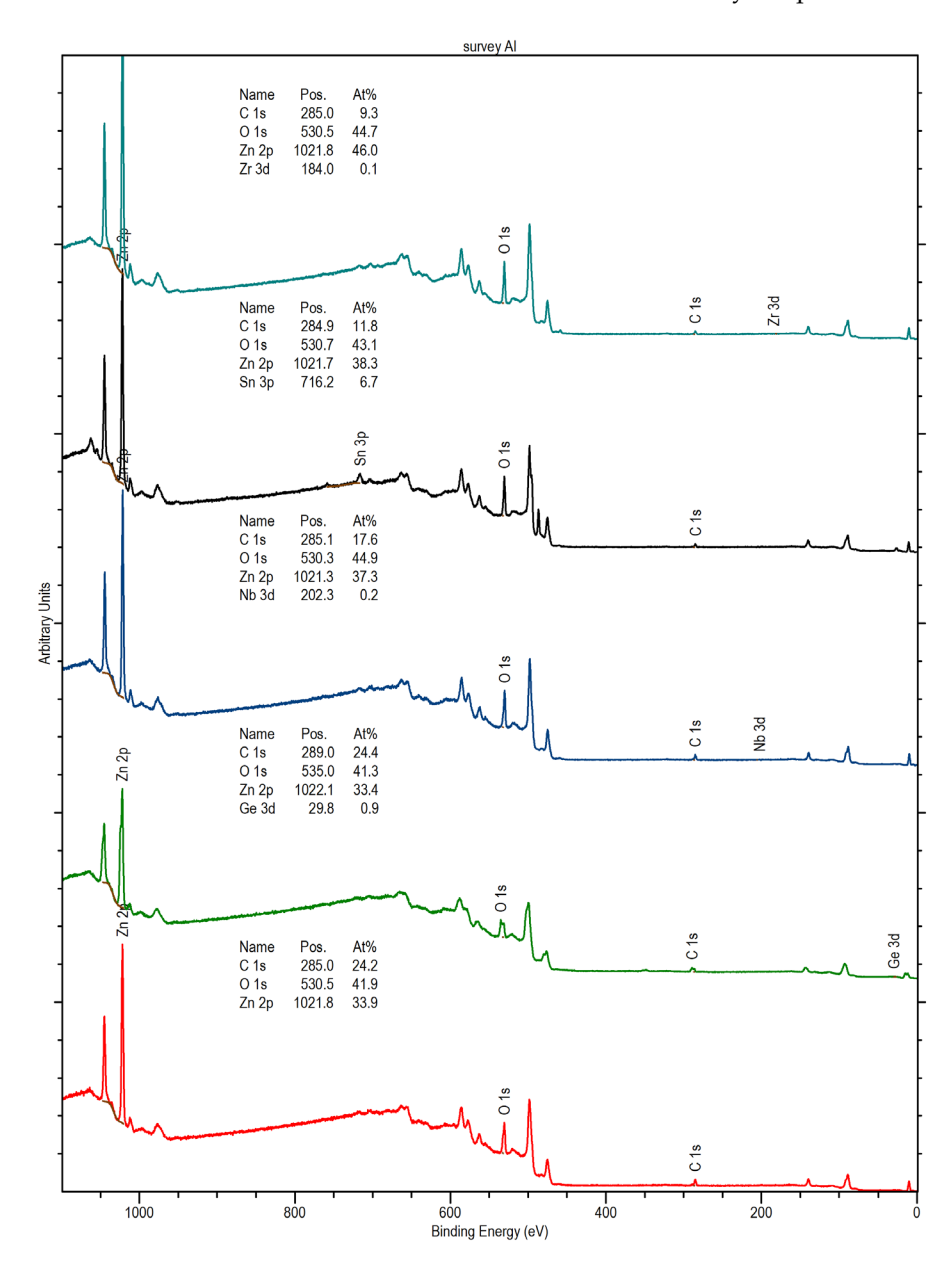


Figure 5. XPS measurement results for ZZO, SZO, NZO, GZO and ZnO (top to bottom).

The atomic concentration was calculated for the thickness of the surface layer of 5.5 and 8.4 nm, respectively, for ZnO and C. The calculations were performed with QUASES-IMFP-TPP2M Ver 2.2 software according to S. Tanuma, C.J. Powell, D.R. Penn, Surf. Interf. Anal. 21 (1993) 165. The calculations take into account 95% of the photoelectrons emitted from the surface. The accuracy of the calculation is $\pm 3\%$. The number and components' contributions are dependent on the deconvolution procedure. The procedure takes into account the following: the lowest number of components, FWHM related to physically possible values for the given elements, analyzer resolution, and the chemical composition of the samples. The chemical states are assigned to certain peaks according to the databases in [83,84].

The results of the XPS measurement showed that expected doping levels did not match with real concentrations of additives in the tested samples. As shown in Table 2, the doping levels varied at 0.9, 6.7, 0.1 and 0.2 At%, respectively, for germanium, tin, zirconium and niobium doping. The high doping level of the SZO layer could be the reason for the significant changes in refractive index and layer thickness.

Spectrum Component	ZnO	GZO	SZO	ZZO	NZO
C 1s	24.2 At%	24.4 At%	11.8 At%	9.3 At%	17.6 At%
O 1s	41.9 At%	41.3 At%	43.1 At%	44.7 At%	44.9 At%
Zn 2p	33.9 At%	33.4 At%	38.3 At%	46.0 At%	37.3 At%
Ge 3d	-	0.9 At%	-	-	-
Sn 3p	-	-	6.7 At%	-	-
Zr 3d	-	-	-	0.1 At%	-
Nb 3d	-	-	-	-	0.2 At%

Table 2. Atomic composition of deposited layers calculated from XPS spectra.

In all samples, a high carbon content (C 1s) is observed at the surface. In the ZnO layer, the carbon share is 25.2 At%, which suggests that zinc precursor (DEZ) does not react completely during the ALD process, and some organic adsorbate is present at the deposited layer. In doped layers (except for GZO), a carbon content is lower than in the pure ZnO layer, which suggests that dopant pulses react with undecomposed organic residues from ZnO pulses, lowering overall carbon content. This mechanism could consist of one of two phenomena: first, a reaction between the not completely decomposed zinc precursor with the metal doping precursor, resulting in the formation of Zn-doping metal bounding, or second, a reaction of a not completely decomposed zinc precursor with excess water from the doping pulse, leading to the formation of ZnO.

Deconvoluted spectra of doping elements (shown in Figure 6) deliver more information about the differences between the tested layers. Germanium in GZO is present in the form of GeO_x with an oxidation state lower than +4, which implicates that some part of the Ge precursor might not decompose completely, which could explain the higher carbon content than other doped layers. Tin in SZO occurs in a +4 oxidation state in the form close to SnO_2 . Zirconium, similar to germanium, occurs in an oxidation state below +4 in the form of ZrO_x , but with oxygen vacancies and not as in case of GZO with organic parts, which might explain the much lower carbon content in the SZO layer. Niobium in the NZO layer exhibits +5 oxygen state and occurs in a form very close to stoichiometric oxide Nb_2O_5 .

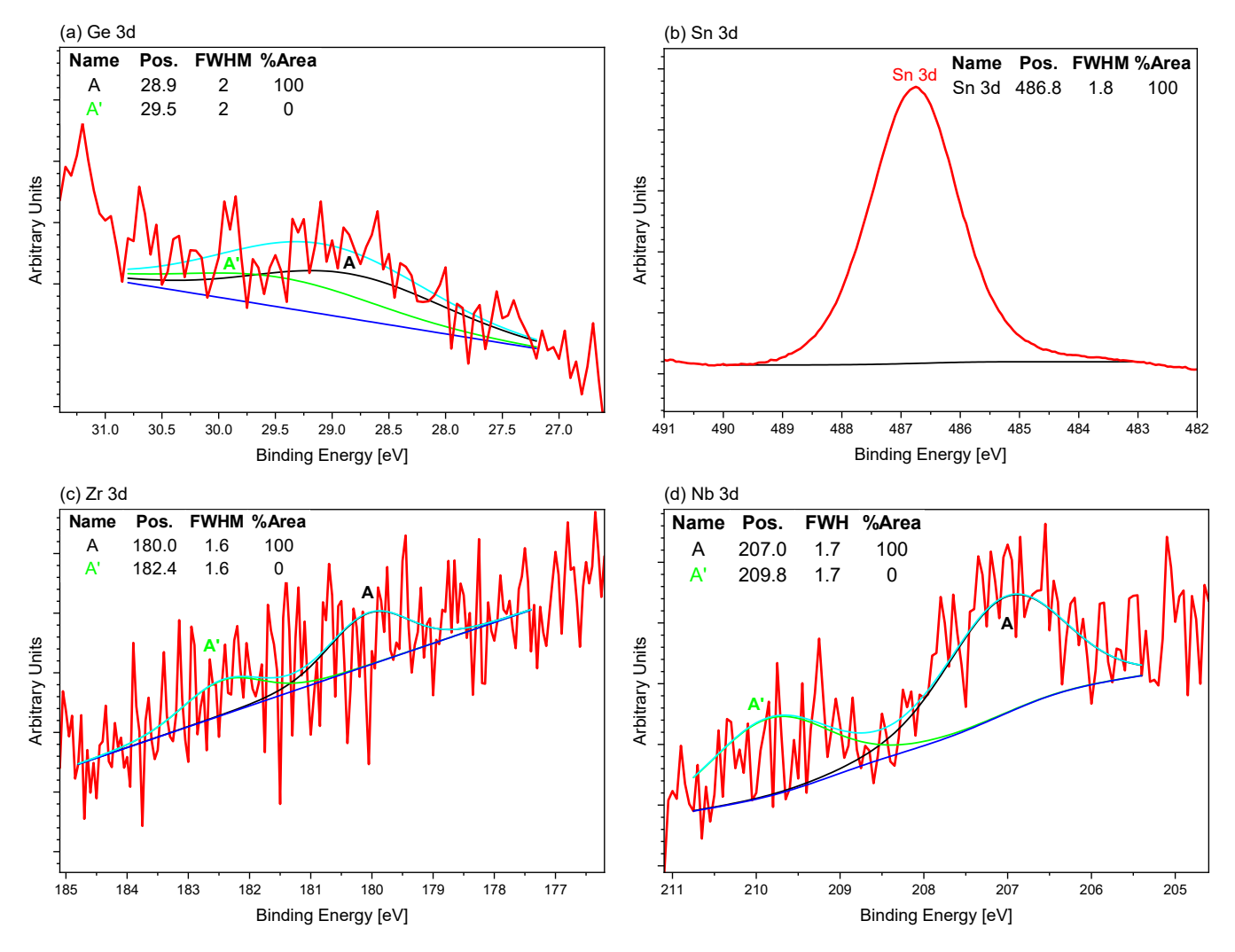


Figure 6. Deconvoluted spectra of (a) Ge 3d, (b) Sn 3d, (c) Zr 3d and (d) Nb 3d.

To investigate the electrical properties of doped films, Hall effect measurements were conducted. Results of performed measurements are presented below in Table 3.

Table 3. Electrical properties of deposited layers obtained from the Hall measurement system.

Sample Name	Sheet Carrier Concentration [cm ⁻²]	Sheet Resistance $[\Omega/\Box]$	Resistivity [Ωcm]	Conductivity [1/Ωcm]	Mobility [cm²/Vs]
ZnO	6.3×10^{13} (n)	$2.0 imes 10^4$	$2.0 imes 10^{-1}$	5.0×10^{0}	4.922
GZO	2.8×10^{15} (n)	$2.4 imes 10^2$	$2.4 imes 10^{-3}$	$4.2 imes 10^2$	9.559
SZO	1.8×10^{14} (n)	3.1×10^{5}	3.1×10^{0}	3.3×10^{-1}	0.122
ZZO	1.8×10^{15} (n)	2.6×10^{2}	2.6×10^{-3}	3.8×10^{2}	12.962
NZO	4.7×10^{14} (n)	5.1×10^{2}	5.1×10^{-3}	2.0×10^{2}	26.156

All of the tested samples, including undoped zinc oxide, were found to be n-type semiconductors. For all doped samples, the carrier concentration increases compared to pristine ZnO. Besides their high doping level, SZO layers have the smallest carrier concentration among the tested doping variants. Taking into account the rise in the sheet resistance as well compared to undoped ZnO, it can be suggested that tin doping in a ZnO layer is not completely distributed into the crystal lattice, but instead forms SnO₂ agglomerates, which is consistent with the results from XPS measurements. The formation

of $\rm SnO_2$ structures in the SZO film would explain the lower-than-expected carrier density and hindered carrier transport (which results in the higher resistance). The highest carrier concentration at 2.8×10^{15} was obtained for the germanium-doped sample, which is due to the highly effective doping level. The second highest carrier concentration, besides having the smallest effective doping level, was observed for ZZO samples. High influence of zirconium doping on carrier concentration in ZZO layers might be due to the very successful incorporation of Zr atoms into ZnO lattice (creating oxygen vacancies). The proper incorporation of zirconium into a zinc oxide layer is also demonstrated by the small carbon content in the XPS spectrum of ZZO. The influence of niobium doping on ZnO appears similar to that of tin, but because of the small doping level and higher oxidation stage, even if some part of Nb doping forms Nb₂O₅ clusters, their impact is not sufficient to completely hinder the effects of Nb atoms incorporated into the lattice.

The electron mobility of deposited layers corresponds to their conductivity, in line with the following equation:

$$\sigma = q \cdot n \cdot \mu \tag{2}$$

where σ —electrical conductivity [1/ Ω cm]; q—charge of an electron (1.6 · 10⁻¹⁹ C); n—carrier concentration [cm⁻³]; and μ —carrier mobility [cm²/Vs].

The highest mobility was observed for niobium-doped samples 26.156 cm²/Vs and the lowest mobility was observed for SZO layer 0.122 cm²/Vs. Besides having a similar doping level, for both samples, the difference in carrier mobility is huge; this may be caused by the presence of carrier traps or uneven carrier distribution along the layer in tin-doped samples. In ZZO layers, mobility is less than half of NZO mobility with a conduction value close to that of niobium, which, according to Equation (2), is related to a higher carrier doping level [85,86]. In the case of the GZO and pure ZnO layer, besides having lower and higher carrier concentrations (and conductivity), both samples have lower mobility than zirconium-doped variants. This may be caused by the high carbon content in this layer, derived from traces of organic precursors, which could suppress the free movement of the carrier inside the layer.

To further investigate doping influence on ZnO properties, band gap calculations using the Tauc plot method were conducted (Figure 7). For all tested variants, the band gap (bg) energy increases, wherein the highest change is observed for GZO at 3.50 eV (Table 4). There are visible correlations between sheet carrier concentrations from the Hall effect measurement and the obtained band gap energies. This phenomena could be caused by the Burstein–Moss effect (BM). The increased carrier concentration caused by metal doping in n-type semiconductors shifts the Fermi level towards the conduction band. With the electrons from doped atoms filling the band, free states in the conduction band move to higher energy levels, resulting in a band gap energy increase [87,88]. The same effect was observed in the work of Sahayaraj with increasing germanium doping content (0, 5, 10, 20 and 30%). In ZnO thin layers, blue shifts were observed, ranging from 3.26 eV for undoped ZnO to 3.82 eV for a 30% doping level. After plotting the band gap energy against carrier density, a nearly linear correlation was observed [70]. Besides BM, the size of the change in band gap could also have been influenced by effective doping levels. The highest change in band gap was observed for GZO, which had a high effective doping content of 0.9%. The niobium doping level was very low, which resulted in a small increase in band gap energy. Zirconium doping was very effective at influencing ZnO layers, whereby even a low concentration of 0.2% results in high carrier concentration (1.8 \times 10¹⁵ cm⁻²). SZO samples, despite having the highest doping level of 6.7%, had a band gap energy closest to pristine ZnO; this may have been related to the agglomeration of tin doping, which, instead of incorporation into ZnO lattice crate as SnO₂ clusters, these clusters were not visible on

the UV-Vis spectrum of the sample because of the wider band gap of 3.6 eV [89] than ZnO 3.23 eV (this work).

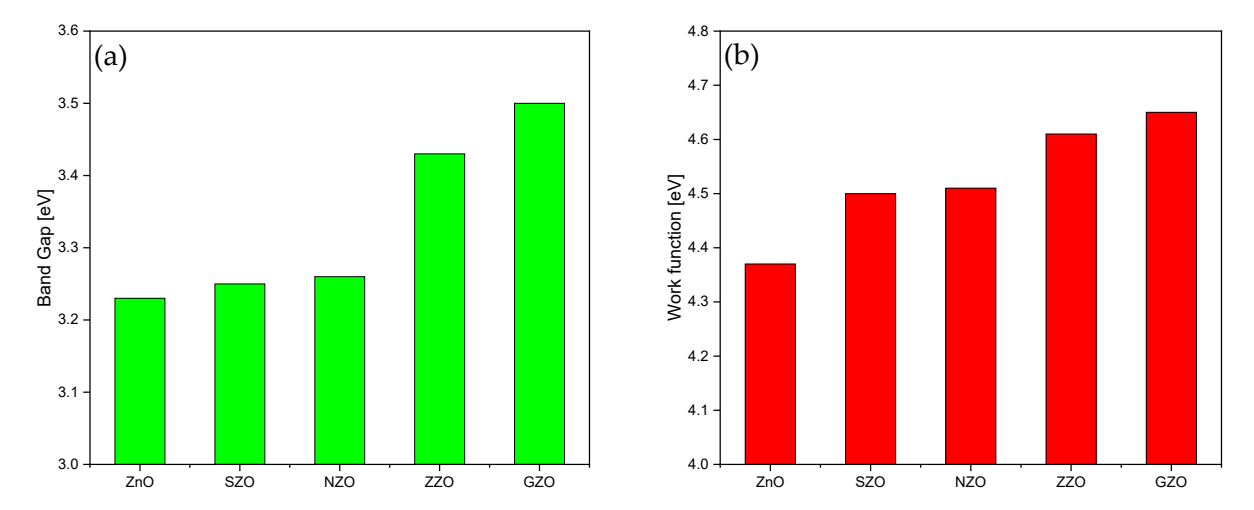


Figure 7. (a) Band gap calculated from Tauc plot. (b) Work function calculated from Kelvin probe measurement.

Table 4. Band gap energy and work function of deposited layers.

Sample Name	ZnO	SZO	NZO	ZZO	GZO
Band gap energy [eV]	3.23	3.25	3.26	3.45	3.50
Work function [eV]	4.37	4.50	4.51	4.61	4.65

Work function (WF) calculated from Kelvin probe measurements shares the same trends as the band gap. For all tested samples, the WF increases with carrier concentration ranging from 4.37 for undoped ZnO to 4.65 for the germanium-doped layer (Table 4). Considering close connection between WF and the fermi level, this result could prove the earlier assumption of the influence of the Burstein–Moss effect on the energy gap.

Work function is mostly associated with an electron energy level on the surface of a measured sample. In semiconductors, the electron energy level, besides electron affinity, is mostly dependent on the carrier concentration (doping level). In case of doped oxides, electron doping at their surfaces is caused by the surface oxygen vacancies; thus, in case of oxide semiconductors layers, a rise in their work function will be related to the increase in oxygen vacancies at the surface (and probably also in bulk material). The quantity of oxygen vacancies will determine the amount of oxygen species which, in turn, will be able to adsorb to the surface or migrate into the material filing oxygen vacancies. This may result in the rise in the layer resistance (sensor response) [90].

Before sensor testing, deposited layers were annealed and gold contacts were deposited (exact descriptions are mentioned in Section 2). The contacts were deposited in such a way that the distance between them was 2.5 ± 0.1 mm. In the initial tests of developed sensors, following the oxygen introduction step, an increase in the sensor resistance was observed in a nitrogen atmosphere, even after a prolonged period. This suggests that the deposited layers were not stable under the testing conditions and required additional treatment. To stabilize the sensors, the annealing process in an oxygen atmosphere was additionally introduced. During this process, deeper oxygen vacancies are filled, and all organic residues within the tested layers that did not decompose during the deposition process are removed. An annealing temperature of 500 °C was selected to exceed the temperatures applied during the sensor testing procedure. The process time was experimentally set at 3 h, as the resistance increase phenomenon persisted after 1 and 2 h of

annealing. After annealing, only SZO and GZO devices were suitable for sensor testing, and the rest of the samples became too resistive for a used sensor testing system, probably due to the filling of oxygen vacancies responsible for conduction in ZnO films (maximum resistance measured by the sensor testing system < $60 \text{ M}\Omega$).

Sensor testing was conducted using the constructed system presented in Figure 4. In order to deliver thermal energy for chemisorption and diffusion of oxygen specimen into the sensor's active layer, the devices were heated and tested at varied temperatures, including 250 °C, 300 °C, 350 °C, 400 °C and 450 °C; the temperature range was chosen based on system capabilities and previous experience. The procedure consisted of heating the sample in nitrogen flow (N_2 obtained from nitrogen generator 99.999% purity, PSA Nitrogen Gas Generator, Parker) after establishing a constant resistance value (N_2 sensor resistance); 90% purity dry oxygen was introduced into the chamber to replace nitrogen, and after establishing a constant resistance value, the O_2 sensor resistance was obtained. This procedure was executed for all chosen temperatures; after collecting data, the responses of the sensors were calculated using Equation (3):

$$Response = \frac{R_{O_2}}{R_{N_2}} \tag{3}$$

where R_{O2} is the sensor resistance with oxygen flow through the testing chamber, and R_{N2} is the sensor resistance with nitrogen flow through the testing chamber.

The results of sensor testing are shown in Figure 8. It can be observed that both of the tested devices exhibit sensor properties. The device based on the SZO layer responded with a range from 1.19 to 3.14, which increases with the temperature increase. For GZO-based sensor, the minimal working temperature is 350 °C; below this temperature, the sensor response is below 1.10, which is not enough for a reliable sensor performance. At 350 °C, the response of the device reaches 1.75, which is acceptable (Table 5). The GZO sensor works the best at temperatures exceeding 350 °C; after this point, the response of the sensor grows quickly, achieving 12.32 and 88.21 responses at 400 and 450 °C, respectively. Among the tested sensors, SZO devices work better at low temperature, whereas at high temperatures, the GZO sensor significantly outperforms the SZO sensor.

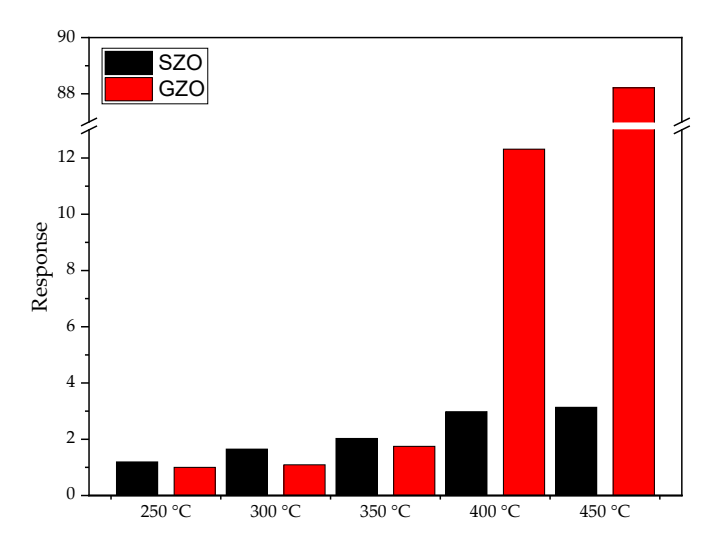


Figure 8. Response of tested sensors in different temperatures.

Table 5. Response of fabricated sensor devices in variable temperature.

	250 °C	300 °C	350 °C	400 °C	450 °C
GZO	1.00	1.10	1.75	12.32	88.21
SZO	1.19	1.65	2.03	2.98	3.14

A major drawback of fabricated devices is their long sensing and recovery times, often longer than 180 s. This issue may stem from the thickness of the tested layers. A thinner sensor would probably fill (or empty) all oxygen vacancies faster and reach constant resistance.

The differences between the behavior of presented SZO and GZO devices may result from the stability constant K_f of applied dopants. In the case of germanium, the formation of two oxides is allowed, i.e., GeO₂ and GeO, while data obtained from XPS deconvolution spectra demonstrate that in GZO layers, germanium oxide is in the oxidation state lower than +4, which may suggest that some of the germanium precursor is left in the layer or that some of germanium oxide occurs in the form of GeO. The presence of these two oxides in GZO devices could explain the increased response at high temperatures. At low temperatures, GeO, with a lower stability constant ($K_f = 8 \times 10^{21}$, given for 450 °C for clarity) is responsible for the interaction with oxygen species. However, due to its low content, the response remains very weak. At higher temperatures, the second oxide GeO₂ (with a significantly higher stability constant $K_f = 5 \times 10^{31}$) becomes active and, due to its much higher concentration, results in a much stronger response. In the case of SZO devices, tin oxide exists predominantly in an oxidation state close to +4, resembling SnO₂. The absence of a second oxide form could explain the linear increase in response ($R^2 = 0.96$). The better performance of SZO devices at lower temperatures might be attributed to the lower stability constant of SnO₂ ($K_f = 6 \times 10^{30}$) compared to GeO₂ and the higher overall content of GeO (stability constant of oxides were calculated by FactSage© 8.2 software using the built-in database and another material database from [91]). The differences in response at higher temperatures could be related to variations in dopant incorporation into the ZnO crystal lattice. Smaller changes in the optical band gap and work function suggest that tin doping leads to the formation of agglomerates (likely due to the high doping level) in the deposited layers, which results in a limited number of defects. Hall measurements confirm this effect, as they show a low carrier density and high resistance.

The obtained results are several times bigger than those reported for other sensors found in the literature (Table 6), the majority of oxygen sensor devices based on doped ZnO do not exceed the sensor response at a level of 2. Another advantage of the solution shown is the relatively low working temperature compared to other oxygen sensors in the literature [8]. Rajput, J.K. et al. reported the fabrication of a device that exhibited a response exceeding 100 at a relatively low temperature of 150 °C. This high response was attributed to the incorporation of water (60% humidity) into pure oxygen, which likely reacted with the sensor surface. This interaction, combined with oxygen, significantly increased the sensor's response [92]. Layers deposited via ALD replicate the surface morphology of the substrate. In the case of ultra-flat substrates, such as quartz glass or silicon wafers, this results in a very low active surface area for the device fabricated using this method. In contrast, methods commonly reported in the literature, such as wet chemical techniques or magnetron sputtering, are independent of the substrate's surface morphology and can produce highly developed surfaces, enhancing the sensor response. In the future, the development of ALD oxygen sensors should focus on substrate modification to increase surface roughness, thereby improving the active surface area and enhancing the overall sensor performance. As shown, ZnO-doped layers fabricated by the ALD technique have great potential to be the future of resistive oxygen sensors.

Sensor	Working Temperature	Oxygen Concentration	Response	Ref.
$Zn_{0.9}Cu_{0.1}O$	400 °C	33%	1.60	[93]
$Zn_{0.9}Al_{0.1}O$	600 °C	33%	1.20	[93]
$Zn_{0.75}Cd_{0.25}O$	32 °C	100% 60% RH	0.96	[92]
$Zn_{0.25}Cd_{0.75}O$	150 °C	100% 60% RH	102.97	[92]
$Zn_{0.9}Al_{0.01}O$	300 °C	21%	1.30	[94]
GZO	450 °C	90%	88.21	This work
SZO	450 °C	90%	3.14	This work

Table 6. Comparison between response and working temperatures from the literature.

Despite the very high response and low operating temperature compared to other ROS devices described in the literature, the developed sensors exhibit a significantly long response time, ranging from several hundred seconds. In contrast, the literature reports indicate response times typically ranging from a few seconds to a few dozen seconds [95–98]. Resistive sensors described in the literature operate across a wide range of oxygen concentrations, from a few ppm to 100% [99,100]. In this study, a 90% oxygen concentration was used to evaluate sensor performance. However, given the very high response of the GZO sensor, it can be assumed that it would also function effectively at lower oxygen concentrations.

4. Conclusions

This study investigated the impact of four distinct dopants on ZnO layers fabricated via atomic layer deposition (ALD). Comprehensive analyses of chemical composition and electrical properties revealed that germanium doping had the most pronounced effect on ZnO layer characteristics among all tested variants. Despite employing an identical deposition process, variations in effective doping levels were observed across the samples.

Notably, only the germanium-doped ZnO (GZO) and tin-doped ZnO (SZO) devices were suitable for sensor testing. Both sensors demonstrated exceptional oxygen detection capabilities, surpassing other sensors reported in the literature. The proposed devices with response values of 3.14 and 88.21 for SZO and GZO sensors, respectively, outperform other ZnO-based sensors in the literature [92–94] or even other types like the popular cerium oxide, whose response level often reaches about 1.5 or lower [95,101]. It should be noted that the presented ALD layers are almost completely flat, which results in much lower active surface then commonly used sensors with very rough, complex surfaces, providing many more surface oxygen vacancies and allowing us to reach higher responses. Even with this disadvantage, they still outperformed other sensors. Furthermore, they operated efficiently at relatively low temperatures, addressing a common challenge associated with this type of sensor.

These findings confirm that ZnO layers doped via ALD hold significant potential as future resistive oxygen sensors. Future research may focus on optimizing the doping process and elucidating the mechanisms responsible for enhanced sensitivity and selectivity in these sensors. It is noteworthy that previous studies on doping ZnO with various elements, such as aluminum, have shown significant improvements in the optical and electrical properties of ZnO layers. For instance, aluminum doping (AZO) has been found to enhance the conductivity and transparency of ZnO layers, which is advantageous for applications in electronics and optoelectronics. Similarly, research on the influence of aluminum doping on the morphology, structure and sensor properties of ZnO layers has indicated that appropriate dopant concentrations can lead to improved gas sensor sensitivity. These observations suggest that selecting suitable dopants and controlling

their concentrations in ZnO layers are crucial for the development and optimization of ZnO-based oxygen sensors.

Author Contributions: Conceptualization, W.B., R.P.S. and M.W.; methodology, W.B, R.P.S., A.D., P.K., P.P. and M.W.; validation, A.D., P.K. and M.W.; formal analysis, W.B, R.P.S. and P.P.; investigation, W.B, R.P.S., A.D., P.P. and M.W.; resources, R.P.S. and M.W.; data curation, W.B. and A.D.; writing—original draft preparation, W.B.; writing—review and editing, R.P.S. and A.D.; supervision, R.P.S. and M.W.; project administration, M.W.; funding acquisition, R.P.S. and M.W. All authors have read and agreed to the published version of the manuscript.

Funding: This research was funded by Polish Ministry of Science and Education, grant number DWD/7/0287/2023.

Data Availability Statement: The data presented in this study are available on request from the corresponding author.

Acknowledgments: I would like to express my sincere gratitude to the Ministry of Education and Science for granting the Implementation PhD Program. This opportunity has been instrumental in advancing my research and professional development.

Conflicts of Interest: The authors declare no conflicts of interest.

References

- 1. Johny, V.; Chinmaya, K.V.; Nihal, C.V.M.; Kurian, V.; Rao, G.M.; Ghosh, M.; Ghosh, S. Towards Real-Time Oxygen Sensing: From Nanomaterials to Plasma. *Front. Sens.* **2022**, *2*, 21. [CrossRef]
- 2. Kashem, M.A.; Suzuki, M.; Kimoto, K.; Iribe, Y. An Optical Biochemical Oxygen Demand Biosensor Chip for Environmental Monitoring. *Sens. Actuators B Chem.* **2015**, 221, 1594–1600. [CrossRef]
- 3. Ardi, S.; Abdurrahman, H. Design of Pokayoke Systems to Increase the Efficiency of Function Check Oxygen Sensor Machine Using Programmable Logic Controller in Manufacturing Industry. In Proceedings of the 2017 4th International Conference on Information Technology, Computer, and Electrical Engineering (ICITACEE), Semarang, Indonesia, 18–19 October 2017; pp. 192–196.
- 4. Ramamoorthy, R.; Dutta, P.K.; Akbar, S.A. Oxygen Sensors: Materials, Methods, Designs and Applications. *J. Mater. Sci.* **2003**, *38*, 4271–4282. [CrossRef]
- 5. Tutunea, D.; Dumitru, I.; Stănciuc-Oţăt, O. V Overview of the Use of Oxygen Sensors in Automotive Applications. *IOP Conf. Ser. Mater. Sci. Eng.* **2024**, 1303, 012014. [CrossRef]
- 6. Liu, J.; Zhang, X.; Zhu, S.; Li, X.; Zhao, H.; Li, X.; Zhang, H.; Jiang, H.; Lu, X.; Kong, W.; et al. Development and Measurement of Airborne Oxygen Sensor for Aircraft Inerting System Based on TDLAS with Pressure Compensation and 2f/1f Normalized Method. *Infrared Phys. Technol.* 2023, 131, 104689. [CrossRef]
- 7. Yuan, M.; Zhang, X.; Wang, J.; Zhao, Y. Recent Progress of Energy-Storage-Device-Integrated Sensing Systems. *Nanomaterials* **2023**, 13, 645. [CrossRef]
- 8. Bulowski, W.; Knura, R.; Socha, R.P.; Basiura, M.; Skibińska, K.; Wojnicki, M. Thin Film Semiconductor Metal Oxide Oxygen Sensors: Limitations, Challenges, and Future Progress. *Electronics* **2024**, *13*, 3409. [CrossRef]
- 9. Jasek, K.; Pasternak, M.; Grabka, M. Paramagnetic Sensors for the Determination of Oxygen Concentration in Gas Mixtures. *ACS Sens.* **2022**, *7*, 3228–3242. [CrossRef]
- 10. Orlov, S.N.; Bogachev, N.A.; Mereshchenko, A.S.; Zmitrodan, A.A.; Skripkin, M.Y. Electrochemical Sensors for Controlling Oxygen Content and Corrosion Processes in Lead-Bismuth Eutectic Coolant—State of the Art. *Sensors* 2023, 23, 812. [CrossRef]
- 11. Nashimoto, Y.; Mukomoto, R.; Imaizumi, T.; Terai, T.; Shishido, S.; Ino, K.; Yokokawa, R.; Miura, T.; Onuma, K.; Inoue, M.; et al. Electrochemical Sensing of Oxygen Metabolism for a Three-Dimensional Cultured Model with Biomimetic Vascular Flow. *Biosens. Bioelectron.* 2023, 219, 114808. [CrossRef]
- 12. Liu, Y.; Gao, L.; Cheng, T.; Zhang, X.; Li, Y.; Zhang, X.; Zheng, W.; Wang, Y.; Zhang, J. Lead-Free Double Perovskite Halide Fluorescent Oxygen Sensor with High Stability. *Ceram. Int.* **2023**, 49, 30266–30272. [CrossRef]
- 13. Ge, X.; Kostov, Y.; Rao, G. High-Stability Non-Invasive Autoclavable Naked Optical CO2 Sensor. *Biosens. Bioelectron.* **2003**, *18*, 857–865. [CrossRef] [PubMed]
- 14. Nisti, A.; Dini, F.; Catini, A.; Capuano, R.; Martinelli, E.; Paolesse, R.; Di Natale, C.; D'Amico, A. An Optical Sensor for Measuring Oxygen Concentration. In *Sensors*; Springer: New York, NY, USA, 2014; pp. 459–463.

15. Moos, R.; Izu, N.; Rettig, F.; Reiß, S.; Shin, W.; Matinfara, I. Resistive Oxygen Gas Sensors for Harsh Environments. *Sensors* **2011**, 11, 3439–3465. [CrossRef] [PubMed]

- 16. Franco, M.A.; Conti, P.P.; Andre, R.S.; Correa, D.S. A Review on Chemiresistive ZnO Gas Sensors. *Sens. Actuators Rep.* **2022**, 4, 100100. [CrossRef]
- 17. Kang, X.; Deng, N.; Yan, Z.; Pan, Y.; Sun, W.; Zhang, Y. Resistive-Type VOCs and Pollution Gases Sensor Based on SnO2: A Review. *Mater. Sci. Semicond. Process* **2022**, *138*, 106246. [CrossRef]
- 18. Li, Z.; Yao, Z.; Haidry, A.A.; Plecenik, T.; Xie, L.; Sun, L.; Fatima, Q. Resistive-Type Hydrogen Gas Sensor Based on TiO2: A Review. *Int. J. Hydrog. Energy* **2018**, *43*, 21114–21132. [CrossRef]
- 19. Shu, L.; Wang, X.; Yan, D.; Fan, L.; Wu, W. The Investigation of High-Temperature SAW Oxygen Sensor Based on ZnO Films. *Materials* **2019**, 12, 1235. [CrossRef] [PubMed]
- 20. Hu, Y.; Tan, O.K.; Pan, J.S.; Huang, H.; Cao, W. The Effects of Annealing Temperature on the Sensing Properties of Low Temperature Nano-Sized SrTiO3 Oxygen Gas Sensor. *Sens. Actuators B Chem.* **2005**, *108*, 244–249. [CrossRef]
- 21. Duan, C.; Zhang, L.; Wu, Z.; Wang, X.; Meng, M.; Zhang, M. Study on the Deterioration Mechanism of Pb on TiO2 Oxygen Sensor. *Micromachines* **2023**, *14*, 156. [CrossRef] [PubMed]
- 22. Wawrzyniak, J. Advancements in Improving Selectivity of Metal Oxide Semiconductor Gas Sensors Opening New Perspectives for Their Application in Food Industry. *Sensors* **2023**, 23, 9548. [CrossRef] [PubMed]
- 23. Li, J.; Zhao, H.; Wang, Y.; Zhou, Y. Approaches for Selectivity Improvement of Conductometric Gas Sensors: An Overview. *Sens. Diagn.* **2024**, *3*, 336–353. [CrossRef]
- Barhoum, A.; Hamimed, S.; Slimi, H.; Othmani, A.; Abdel-Haleem, F.M.; Bechelany, M. Modern Designs of Electrochemical Sensor Platforms for Environmental Analyses: Principles, Nanofabrication Opportunities, and Challenges. *Trends Environ. Anal. Chem.* 2023, 38, e00199. [CrossRef]
- Hakeem Anwer, A.; Saadaoui, M.; Mohamed, A.T.; Ahmad, N.; Benamor, A. State-of-the-Art Advances and Challenges in Wearable Gas Sensors for Emerging Applications: Innovations and Future Prospects. Chem. Eng. J. 2024, 502, 157899. [CrossRef]
- 26. Huang, Y.-H.; Yen, T.-Y.; Shi, M.-T.; Hung, Y.-H.; Chen, W.-T.; Wu, C.-H.; Hung, K.-M.; Lo, K.-Y. Competition between Oxygen and Water Molecules on SiO2/P-Doped Si Surface: The Electrical Dipole Evolution on Water/Oxygen-Adsorbed Oxide Surface. *Sens. Actuators B Chem.* **2023**, *376*, 133011. [CrossRef]
- 27. Yang, L.-Y.; Ke, T.-S.; Yan, Z.-J.; Yeh, C.-H.; Tseng, W.J. Effect of Humidity Interference on NO2 Gas Sensing of In2O3 Nanoneedles at Moderate Operating Temperature. *Ceram. Int.* **2024**, *50*, 38415–38423. [CrossRef]
- 28. Tereshkov, M.; Dontsova, T.; Saruhan, B.; Krüger, S. Metal Oxide-Based Sensors for Ecological Monitoring: Progress and Perspectives. *Chemosensors* **2024**, *12*, 42. [CrossRef]
- 29. Fuśnik, Ł.; Szafraniak, B.; Paleczek, A.; Grochala, D.; Rydosz, A. A Review of Gas Measurement Set-Ups. *Sensors* **2022**, 22, 2557. [CrossRef] [PubMed]
- 30. Robbiani, S.; Lotesoriere, B.J.; Dellacà, R.L.; Capelli, L. Physical Confounding Factors Affecting Gas Sensors Response: A Review on Effects and Compensation Strategies for Electronic Nose Applications. *Chemosensors* **2023**, *11*, 514. [CrossRef]
- 31. Recent, Y.; Kulinich, S.; Wang, Y.; Zhou, Y. Recent Progress on Anti-Humidity Strategies of Chemiresistive Gas Sensors. *Materials* **2022**, *15*, 8728. [CrossRef]
- 32. Korotcenkov, G.; Boris, I.; Brinzari, V.; Han, S.H.; Cho, B.K. The Role of Doping Effect on the Response of SnO2-Based Thin Film Gas Sensors: Analysis Based on the Results Obtained for Co-Doped SnO2 Films Deposited by Spray Pyrolysis. *Sens. Actuators B Chem.* 2013, 182, 112–124. [CrossRef]
- 33. Jeong, S.; Moon, Y.K.; Kim, J.K.; Park, S.; Jo, Y.K.; Kang, Y.C.; Lee, J. A General Solution to Mitigate Water Poisoning of Oxide Chemiresistors: Bilayer Sensors with Tb 4 O 7 Overlayer. *Adv. Funct. Mater.* **2021**, *31*, 2007895. [CrossRef]
- 34. Bernasconi, S.; Angelucci, A.; De Cesari, A.; Masotti, A.; Pandocchi, M.; Vacca, F.; Zhao, X.; Paganelli, C.; Aliverti, A. Recent Technologies for Transcutaneous Oxygen and Carbon Dioxide Monitoring. *Diagnostics* **2024**, *14*, 785. [CrossRef]
- 35. Yu, J.; Wang, D.; Tipparaju, V.V.; Tsow, F.; Xian, X. Mitigation of Humidity Interference in Colorimetric Sensing of Gases. *ACS Sens.* **2021**, *6*, 303–320. [CrossRef] [PubMed]
- 36. Huang, M.; Wang, S.; Fu, H.; Shao, H.; Wang, Y.; Yu, K.; Huang, Y.; Jv, Z.; Wang, L. An Efficient Vapor-Phase Processing Method Derived Mesoporous N-C@SnO2-Co3O4 Hollow Nanoboxes with Abundant Surface Oxygen Vacancy for Highly Improved Gas Sensing Application. *J. Alloys Compd.* **2021**, *863*, 158341. [CrossRef]
- 37. Shooshtari, M.; Pahlavan, S.; Rahbarpour, S.; Ghafoorifard, H. Investigating Organic Vapor Sensing Properties of Composite Carbon Nanotube-Zinc Oxide Nanowire. *Chemosensors* **2022**, *10*, 205. [CrossRef]
- 38. Godse, P.R.; Kadam, S.A.; Nimbalkar, T.M.; Jadhav, Y.M.; Jadhao, Y.B.; Ma, Y.R.; Patil, V.B. Ultra-Responsive and Highly Sensitive 1D ZnO Nanotubes for Detecting Perilous Low Levels of NO2 Gas. *Mater. Adv.* **2024**, *5*, 2826–2840. [CrossRef]
- 39. Liu, Y.; Zhang, J.; Li, G.; Liu, J.; Liang, Q.; Wang, H.; Zhu, Y.; Gao, J.; Lu, H. In2O3–ZnO Nanotubes for the Sensitive and Selective Detection of Ppb-Level NO2 under UV Irradiation at Room Temperature. Sens. Actuators B Chem. 2022, 355, 131322. [CrossRef]

40. Al-Salman, H.S.; Abdullah, M.J.; Al-Hardan, N. ZnO Thin Film Nanostructures for Hydrogen Gas Sensing Applications. *Ceram. Int.* **2013**, *39*, S447–S450. [CrossRef]

- 41. Aleksanyan, M.; Sayunts, A.; Aroutiounian, V.; Shahkhatuni, G.; Simonyan, Z.; Shahnazaryan, G. Gas Sensor Based on ZnO Nanostructured Film for the Detection of Ethanol Vapor. *Chemosensors* **2022**, *10*, 245. [CrossRef]
- 42. Khosravi, Y.; Sasar, M.; Abdi, Y. Light-Induced Oxygen Sensing Using ZnO/GO Based Gas Sensor. *Mater. Sci. Semicond. Process* **2018**, *85*, 9–14. [CrossRef]
- 43. Li, S.; Yu, L.; Cao, L.; Zhang, C.; Du, H.; Wang, H.; Fan, X.; Gu, F. Engineering of Thickness Tunable 2D Graphdiyne Film to ZnO Nanowalls via Nanospace-Confined Synthesis Promotes NO2 Gas Sensing Performance. *Sens. Actuators B Chem.* 2024, 410, 135729. [CrossRef]
- 44. Oviroh, P.O.; Akbarzadeh, R.; Pan, D.; Coetzee, R.A.M.; Jen, T.-C. New Development of Atomic Layer Deposition: Processes, Methods and Applications. *Sci. Technol. Adv. Mater.* **2019**, *20*, 465–496. [CrossRef] [PubMed]
- 45. Weber, M.; Julbe, A.; Kim, S.S.; Bechelany, M. Atomic Layer Deposition (ALD) on Inorganic or Polymeric Membranes. *J. Appl. Phys.* **2019**, *126*, 041101. [CrossRef]
- 46. George, S.M. Atomic Layer Deposition: An Overview. Chem. Rev. 2010, 110, 111–131. [CrossRef] [PubMed]
- 47. Johnson, R.W.; Hultqvist, A.; Bent, S.F. A Brief Review of Atomic Layer Deposition: From Fundamentals to Applications. *Mater. Today* **2014**, *17*, 236–246. [CrossRef]
- 48. Yin, Y. Advances and Perspectives of Spin Coating Techniques. Appl. Comput. Eng. 2023, 7, 291–301. [CrossRef]
- 49. Moreira, J.; Vale, A.C.; Alves, N.M. Spin-Coated Freestanding Films for Biomedical Applications. *J. Mater. Chem. B* **2021**, 9, 3778–3799. [CrossRef] [PubMed]
- 50. Nisticò, R.; Scalarone, D.; Magnacca, G. Sol-Gel Chemistry, Templating and Spin-Coating Deposition: A Combined Approach to Control in a Simple Way the Porosity of Inorganic Thin Films/Coatings. *Microporous Mesoporous Mater.* **2017**, 248, 18–29. [CrossRef]
- 51. Xavier, R.; Sivaperuman, K. Review on the of Physical Vapor Deposition on Imminent Chemiresistive Metal Oxide Gas Sensors and Their Future Scope. *Mater. Today Commun.* **2024**, *38*, 107831. [CrossRef]
- 52. Liang, F.; Yang, J.; Zhao, Y.; Zhou, Y.; Yan, Z.; He, J.; Yuan, Q.; Wu, J.; Liu, P.; Zhong, Z.; et al. A Review of Thin Film Electrolytes Fabricated by Physical Vapor Deposition for Solid Oxide Fuel Cells. *Int. J. Hydrog. Energy* **2022**, 47, 36926–36952. [CrossRef]
- 53. Schalk, N.; Tkadletz, M.; Mitterer, C. Hard Coatings for Cutting Applications: Physical vs. Chemical Vapor Deposition and Future Challenges for the Coatings Community. *Surf. Coat. Technol.* **2022**, 429, 127949. [CrossRef]
- 54. Zhang, J.; Zhang, Y.; Fu, Y.; Chen, R.; Li, T.; Hou, X.; Li, H. Research Progress in Chemical Vapor Deposition for High-Temperature Anti-Oxidation/Ablation Coatings on Thermal Structural Composites. *Compos. B Eng.* **2025**, 291, 112015. [CrossRef]
- 55. Vallejos, S.; Di Maggio, F.; Shujah, T.; Blackman, C. Chemical Vapour Deposition of Gas Sensitive Metal Oxides. *Chemosensors* **2016**, *4*, 4. [CrossRef]
- 56. Nur-E-Alam, M.; Maurya, D.K.; Yap, B.K.; Rajabi, A.; Doroody, C.; Bin Mohamed, H.; Khandaker, M.U.; Islam, M.A.; Kiong Tiong, S. Physical-Vapor-Deposited Metal Oxide Thin Films for PH Sensing Applications: Last Decade of Research Progress. *Sensors* 2023, 23, 8194. [CrossRef] [PubMed]
- 57. Vijayakumar; Shivaraj, B.W.; Manjunatha, C.; Abhishek, B.; Nagaraju, G.; Panda, P.K. Hydrothermal Synthesis of ZnO Nanotubes for CO Gas Sensing. *Sens. Int.* **2020**, *1*, 100018. [CrossRef]
- 58. Bhattarai, R.; Ghimire, R.R.; Mulmi, D.D.; Thapa, R.B. Modeling of Gas Sensor Based on Zinc Oxide Thin Films by Feedback Loop Using Operational Amplifier. *Heliyon* **2024**, *10*, e29222. [CrossRef] [PubMed]
- 59. S., K.G.; Kaur, M.; M., S.; Pathak, A.; Gadkari, S.C.; Debnath, A.K. Highly Sensitive NO2 Sensor Based on ZnO Nanostructured Thin Film Prepared by SILAR Technique. *Sens. Actuators B Chem.* **2021**, *335*, 129678. [CrossRef]
- 60. Soltabayev, B.; Ajjaq, A.; Yergaliuly, G.; Kadyrov, Y.; Turlybekuly, A.; Acar, S.; Mentbayeva, A. Ultrasensitive Nitric Oxide Gas Sensors Based on Ti-Doped ZnO Nanofilms Prepared by RF Magnetron Sputtering System. *J. Alloys Compd.* **2023**, 953, 170125. [CrossRef]
- 61. Kim, H.; Hung, N.L.; Ahn, E.; Jung, H.; Kim, D. Synthesis and Gas Sensing Properties of ZnO Nanostructures. *J. Korean Phys. Soc.* **2010**, *57*, 1784–1788. [CrossRef]
- 62. Nguyen, T.; Adjeroud, N.; Guennou, M.; Guillot, J.; Fleming, Y.; Papon, A.-M.; Arl, D.; Menguelti, K.; Joly, R.; Gambacorti, N.; et al. Controlling Electrical and Optical Properties of Zinc Oxide Thin Films Grown by Thermal Atomic Layer Deposition with Oxygen Gas. *Results Mater.* 2020, *6*, 100088. [CrossRef]
- 63. Papadimitriou, D.N. Engineering of Optical and Electrical Properties of Electrodeposited Highly Doped Al:ZnO and In:ZnO for Cost-Effective Photovoltaic Device Technology. *Micromachines* **2022**, *13*, 1966. [CrossRef] [PubMed]
- 64. Jeon, S.; Bang, S.; Lee, S.; Kwon, S.; Jeong, W.; Jeon, H.; Chang, H.J.; Park, H.-H. Structural and Electrical Properties of ZnO Thin Films Deposited by Atomic Layer Deposition at Low Temperatures. *J. Electrochem. Soc.* **2008**, *155*, H738. [CrossRef]
- 65. Meng, X.; Wang, X.; Geng, D.; Ozgit-Akgun, C.; Schneider, N.; Elam, J.W. Atomic Layer Deposition for Nanomaterial Synthesis and Functionalization in Energy Technology. *Mater. Horiz.* **2017**, *4*, 133–154. [CrossRef]

66. Cao, V.A.; Kim, M.; Hu, W.; Lee, S.; Youn, S.; Chang, J.; Chang, H.S.; Nah, J. Enhanced Piezoelectric Output Performance of the SnS ₂/SnS Heterostructure Thin-Film Piezoelectric Nanogenerator Realized by Atomic Layer Deposition. *ACS Nano* **2021**, *15*, 10428–10436. [CrossRef] [PubMed]

- 67. Sharme, R.K.; Quijada, M.; Terrones, M.; Rana, M.M. Thin Conducting Films: Preparation Methods, Optical and Electrical Properties, and Emerging Trends, Challenges, and Opportunities. *Materials* **2024**, *17*, 4559. [CrossRef]
- 68. Sharma, A.; Abdur, R.; Kim, D.; Tripathi, A.K.; Singh, S.; Lee, J.; Yoo, S.-I. Effect of Ge Doping on the Electrical Properties of Amorphous Zn–Sn–O Thin Films. *Curr. Appl. Phys.* **2020**, 20, 1041–1048. [CrossRef]
- 69. Badadhe, S.S.; Mulla, I.S. Effect of Aluminium Doping on Structural and Gas Sensing Properties of Zinc Oxide Thin Films Deposited by Spray Pyrolysis. *Sens. Actuators B Chem.* **2011**, *156*, 943–948. [CrossRef]
- 70. Sahayaraj, S.; Knura, R.; Skibińska, K.; Starowicz, Z.; Bulowski, W.; Gawlińska-Nęcek, K.; Panek, P.; Wojnicki, M.; Iwanek, S.; Majchrowicz, Ł.; et al. Tuning the Optical and Electrical Properties of ALD-Grown ZnO Films by Germanium Doping. *Materials* **2024**, 17, 2906. [CrossRef]
- 71. *ISO* 15472:2010; Surface Chemical Analysis—X-ray Photoelectron Spectrometers—Calibration of Energy Scales. International Organization for Standardization: Geneva, Switzerland, 2010.
- 72. Altowyan, A.S.; Coban, M.B.; Kaynar, U.H.; Hakami, J.; Çin, E.A.; Kaynar, S.C.; Ayvacikli, M.; Can, N. Lattice Distortion Effects Induced by Li+ Co-Doping on ZnO:Tb3+ Phosphors: Photoluminescence and Unusual Hypersensitive ⁵D⁴ → ⁷F⁰ Transition. *Ceram. Int.* **2024**, *50*, 24036–24044. [CrossRef]
- 73. Safeen, K.; Safeen, A.; Arif, D.; Shah, W.H.; Ali, A.; Ali, G.; Hussain, F.; Imran, N.; Ullah Shah, A.; Alataway, A.; et al. Tuning the Optical Properties of ZnO by Co and Gd Doping for Water Pollutant Elimination. *Water (Basel)* **2023**, *15*, 1470. [CrossRef]
- 74. Marinho, J.Z.; de Paula, L.F.; Longo, E.; Patrocinio, A.O.T.; Lima, R.C. Effect of Gd3+ Doping on Structural and Photocatalytic Properties of ZnO Obtained by Facile Microwave-Hydrothermal Method. *SN Appl. Sci.* **2019**, *1*, 359. [CrossRef]
- 75. Habte, A.G.; Hone, F.G.; Dejene, F.B. Influence of Cu-Doping Concentration on the Structural and Optical Properties of SnO ₂ Nanoparticles by Coprecipitation Route. *J. Nanomater.* **2022**, 2022. [CrossRef]
- 76. Dey, B.; Narzary, R.; Chouhan, L.; Bhattacharjee, S.; Parida, B.N.; Mondal, A.; Ravi, S.; Srivastava, S.K. Crystal Structure, Optical and Dielectric Properties of Ag:ZnO Composite-like Compounds. *J. Mater. Sci. Mater. Electron.* **2022**, *33*, 2855–2868. [CrossRef]
- 77. Mohamed Saadon, N.A.F.; Taib, N.I.; Loy, C.W.; Mohamed, Z. Role of Ca2+ Doping on the Enhancement of Dielectric Properties of Sr2–XCaxNiWO6 for Energy Storage Device Application. *Sci. Rep.* **2023**, *13*, 1246. [CrossRef] [PubMed]
- 78. Zhang, C. Study of the Electronic Structure and Optical Properties of Rare Earth Luminescent Materials. *J. Mater. Sci. Chem. Eng.* **2023**, *11*, 8–18. [CrossRef]
- 79. Tan, P.; Huang, X.; Wang, Y.; Xing, B.; Zhang, J.; Hu, C.; Meng, X.; Xu, X.; Li, D.; Wang, X.; et al. Deciphering the Atomistic Mechanism Underlying Highly Tunable Piezoelectric Properties in Perovskite Ferroelectrics via Transition Metal Doping. *Nat. Commun.* 2024, 15, 10619. [CrossRef]
- 80. Jia, J.; Takasaki, A.; Oka, N.; Shigesato, Y. Experimental Observation on the Fermi Level Shift in Polycrystalline Al-Doped ZnO Films. *J. Appl. Phys.* **2012**, *112*, 013718. [CrossRef]
- 81. Wang, W.; Wang, Y.; He, J.; Bai, Z.; Li, G.; Zhang, X.; He, D.; Zhao, H. Effect of Niobium Doping on Excitonic Dynamics in MoSe2. 2d Mater. 2024, 11, 035003. [CrossRef]
- 82. Starowicz, Z.; Zięba, A.; Ostapko, J.; Wlazło, M.; Kołodziej, G.; Jakub Szczerba, M.; Putynkowski, G.; Piotr Socha, R. Synthesis and Characterization of Al-Doped ZnO and Al/F Co-Doped ZnO Thin Films Prepared by Atomic Layer Deposition. *Mater. Sci. Eng. B* **2023**, 292, 116405. [CrossRef]
- 83. Moulder, J.F.; Stickle, W.F.; Sobol, P.E.; Bomben, K. *Handbook of X-Ray Photoelectron Spectroscopy 2nd Ed. Perkin-Elmer Corporation (Physi-Cal Electronics)*, 2nd ed.; Chastain, J., Ed.; Perkin-Elmer Corporation: Eden Prairie, MN, USA, 1992.
- 84. National Institute of Standards and Technology. *NIST X-Ray Photoelectron Spectroscopy Database, NIST Standard Reference Database Number* 20; National Institute of Standards and Technology: Gaithersburg, MD, USA, 2000.
- 85. Kittel, C. *Introduction to Solid State Physics*, 8th ed.; Johnson, S., McFadden, P., Batey, M., Eds.; John Wiley & Sons Inc: Hoboken, NJ, USA, 2005; Volume 1.
- 86. Sze, S.M.; Ng, K.K. Physics of Semiconductor Devices; Wiley: Hoboken, NJ, USA, 2006. [CrossRef]
- 87. Burstein, E. Anomalous Optical Absorption Limit in InSb. Phys. Rev. 1954, 93, 632–633. [CrossRef]
- 88. Moss, T.S. The Interpretation of the Properties of Indium Antimonide. Proc. Phys. Society. Sect. B 1954, 67, 775–782. [CrossRef]
- 89. Kiruthiga, G.; Rajni, K.S.; Geethanjali, N.; Raguram, T.; Nandhakumar, E.; Senthilkumar, N. SnO2: Investigation of Optical, Structural, and Electrical Properties of Transparent Conductive Oxide Thin Films Prepared by Nebulized Spray Pyrolysis for Photovoltaic Applications. *Inorg. Chem. Commun.* 2022, 145, 109968. [CrossRef]
- 90. Ciftyurek, E.; Li, Z.; Schierbaum, K. Adsorbed Oxygen Ions and Oxygen Vacancies: Their Concentration and Distribution in Metal Oxide Chemical Sensors and Influencing Role in Sensitivity and Sensing Mechanisms. *Sensors* **2022**, 23, 29. [CrossRef] [PubMed]
- 91. Barin, I. Thermochemical Data of Pure Substances; Wiley: Hoboken, NJ, USA, 1995. [CrossRef]

92. Rajput, J.K.; Pathak, T.K.; Kumar, V.; Swart, H.C.; Purohit, L.P. CdO:ZnO Nanocomposite Thin Films for Oxygen Gas Sensing at Low Temperature. *Mater. Sci. Eng. B* **2018**, 228, 241–248. [CrossRef]

- 93. Miller, J.B.; Ashok, T.; Lee, S.; Broitman, E. Zinc Oxide-Based Thin Film Functional Layers for Chemiresistive Sensors. *Thin Solid Film.* **2012**, 520, 6669–6676. [CrossRef]
- 94. Ali, D.; Muneer, I.; Butt, M.Z. Influence of Aluminum Precursor Nature on the Properties of AZO Thin Films and Its Potential Application as Oxygen Sensor. *Opt. Mater.* **2021**, *120*, 111406. [CrossRef]
- 95. Mokrushin, A.S.; Simonenko, E.P.; Simonenko, N.P.; Bukunov, K.A.; Sevastyanov, V.G.; Kuznetsov, N.T. Gas-Sensing Properties of Nanostructured CeO2-XZrO2 Thin Films Obtained by the Sol-Gel Method. *J. Alloys Compd.* **2019**, 773, 1023–1032. [CrossRef]
- 96. Mun, T.; Koo, J.Y.; Lee, J.; Kim, S.J.; Umarji, G.; Amalnerkar, D.; Lee, W. Resistive-Type Lanthanum Ferrite Oxygen Sensor Based on Nanoparticle-Assimilated Nanofiber Architecture. *Sens. Actuators B Chem.* **2020**, 324, 128712. [CrossRef]
- 97. Stratulat, A.; Serban, B.-C.; de Luca, A.; Avramescu, V.; Cobianu, C.; Brezeanu, M.; Buiu, O.; Diamandescu, L.; Feder, M.; Ali, S.; et al. Low Power Resistive Oxygen Sensor Based on Sonochemical SrTi0.6Fe0.4O2.8 (STFO40). Sensors 2015, 15, 17495–17506. [CrossRef] [PubMed]
- 98. Chen, C.-Y.; Chang, K.-H. Temperature Independent Resistive Oxygen Sensor Prepared Using Zirconia-Doped Ceria Powders. *Sens. Actuators B Chem.* **2012**, *162*, 68–75. [CrossRef]
- 99. Bektas, M.; Schönauer-Kamin, D.; Hagen, G.; Mergner, A.; Bojer, C.; Lippert, S.; Milius, W.; Breu, J.; Moos, R. BaFe1-XTaxO3-δ—A Material for Temperature Independent Resistive Oxygen Sensors. *Sens. Actuators B Chem.* **2014**, *190*, 208–213. [CrossRef]
- 100. Izu, N.; Itoh, T.; Shin, W.; Matsubara, I.; Murayama, N. The Effect of Hafnia Doping on the Resistance of Ceria for Use in Resistive Oxygen Sensors. *Sens. Actuators B Chem.* **2007**, *123*, 407–412. [CrossRef]
- 101. Murayama, N.; Izu, N.; Shin, W.; Matsubara, I. Resistive Oxygen Gas Sensors Using Cerium Oxide Nanosized Powder. *MRS Proc.* **2004**, *828*, A3.2/K4.2. [CrossRef]

Disclaimer/Publisher's Note: The statements, opinions and data contained in all publications are solely those of the individual author(s) and contributor(s) and not of MDPI and/or the editor(s). MDPI and/or the editor(s) disclaim responsibility for any injury to people or property resulting from any ideas, methods, instructions or products referred to in the content.